SCIENTIFIC CULTURE
www.sci-cult.com

SCIENTIFIC CULTURE, Vol. 12, No. 4, (2026), pp. 10453-10465
Open Access. Online & Print

DOI: 10.5281/zenodo.124261011

AN INTEGRATED DEM-AWARE FRAMEWORK FOR GLACIER MAPPING AND UNCERTAINTY ANALYSIS USING SENTINEL-2 DATA

Roma Mevadawala[1], Seema Mahajan[1]

[1]Department of Computer Engineering, Indus University, Ahmedabad, Gujarat, India

Received: **22/12/2025**
Accepted: **14/02/2026**

Corresponding Author: Roma Mevadawala
(romamevadawala.ce@indusuni.ac.in)

ABSTRACT

Accurate delineation and uncertainty quantification of clean and debris-covered glaciers in the Himalayan region remain challenging due to rugged topography, seasonal snow cover, and spectral ambiguity between supraglacial debris and surrounding bedrock. This study proposes an uncertainty-aware hierarchical Random Forest (RF) framework that integrates Digital Elevation Model (DEM)-derived topographic features, spectral indices, and probabilistic confidence estimation for improved glacier mapping and multi-temporal change detection. Multi-temporal Sentinel-2 Level-2A imagery from July 2020 and July 2025 over the Lahaul–Spiti region, Himachal Pradesh, India, was analyzed using a temporally invariant classification strategy to ensure consistent change analysis. A two-stage hierarchical RF classifier was implemented to: (1) distinguish glacier from non-glacier areas, and (2) sub-classify clean ice from debris-covered ice. Uncertainty quantification was performed using class probability distributions derived from RF ensemble predictions. The proposed framework achieved classification performance with Stage-1 overall accuracy of 91% and Stage-2 F1-scores of 0.89 (clean ice) and 0.94 (debris-covered ice). Uncertainty analysis revealed <0.1% low-confidence pixels, demonstrating framework robustness. The study detected a net glacier area loss of 5.08 km² between 2020 and 2025, representing an 41.1% area reduction. The framework's transferability, low uncertainty, and hierarchical strategy make it suitable for long-term cryospheric monitoring in complex Himalayan terrain and potentially applicable to other high-mountain regions.

Keywords: Uncertainty quantification; Glacier mapping; Debris-covered glaciers; Sentinel-2 Level-2A; Random Forest classification; DEM integration; Hierarchical classification; Climate change; Himalayan cryosphere; Remote sensing

1. INTRODUCTION

1.1 Background and Motivation

Glaciers are sentinel indicators of regional and global climate variability, responding rapidly to temperature and precipitation changes. The Himalayan cryosphere, encompassing approximately 46,000 glaciers distributed across the Hindu Kush–Karakoram–Himalayan (HKH) system, sustains freshwater availability for over 1 billion people across the Indus, Ganga, and Brahmaputra river basins[1][2]. In recent decades, the Himalayan region has experienced accelerated glacier retreat due to rising temperatures and altered precipitation patterns, with consequences for regional hydrological security and downstream water resources[3].

Accurate and consistent glacier monitoring is therefore essential for understanding climate-glacier interactions, quantifying water resource availability, and informing climate adaptation strategies. Traditional field-based glacier surveys are logistically challenging and provide limited spatial coverage in remote, high-altitude environments. Remote sensing has emerged as the primary methodology for large-scale glacier inventory and change detection, enabling systematic monitoring across spatially extensive and temporally dynamic glacier systems[4][5].

1.2 Remote Sensing and Machine Learning Approaches for Glacier Mapping

Previous studies have employed a wide range of remote sensing approaches for glacier mapping, including spectral index–based methods, supervised machine learning algorithms, object-based image analysis, and deep learning techniques. Methods such as Support Vector Machines (SVM), Random Forest (RF), Artificial Neural Networks (ANN), and Convolutional Neural Networks (CNN) have been widely applied to improve glacier delineation, particularly in complex mountainous terrain. The integration of multispectral satellite data with topographic parameters derived from digital elevation models (DEMs) has further enhanced classification performance by reducing misclassification in debris-covered regions [1–5].

Optical satellite data from Landsat and Sentinel-2 missions have enabled routine glacier monitoring at moderate to high spatial resolution (10–30 m). Traditional spectral-index-based approaches, particularly the Normalized Difference Snow Index (NDSI), are effective for mapping clean, perennial glacier ice due to the strong reflectance contrast between snow/ice and surrounding land surfaces [6]. However, NDSI-based methods perform poorly in debris-covered glacier zones, where supraglacial debris composed of rock, sediment, and fine material exhibits spectral characteristics similar to moraines, exposed bedrock, and shadowed areas [7,8]. This limitation is especially critical in the Himalayan region, where debris-covered glaciers are widespread and increasing due to climate-induced glacier retreat and enhanced debris accumulation. As a result, conventional threshold-based techniques often underestimate glacier extent, leading to significant uncertainties in glacier inventories and change detection studies.

To overcome these limitations, machine learning approaches—particularly Random Forest classifiers—have gained increasing attention. RF models effectively capture nonlinear relationships between spectral, topographic, and textural variables and are robust to noise, collinearity, and overfitting. Their ability to integrate multi-source data within a single framework has made them highly suitable for debris-covered glacier mapping. Recent studies report that RF-based approaches significantly outperform traditional methods, achieving overall accuracies above 90% and F1-scores exceeding 0.85 in complex glacierized terrain [9–12].

Despite significant progress in machine learning–based glacier mapping, several important knowledge gaps remain. Most existing studies primarily report point-based classification accuracies and provide limited insight into spatial and temporal uncertainty patterns, particularly in spectrally complex debris-covered glacier zones [13]. In addition, multi-temporal glacier analyses are often performed using independently trained models, which can introduce inconsistencies and reduce the reliability of glacier change detection. Although the integration of topographic variables derived from DEMs has been shown to improve classification performance, optimal strategies for incorporating such information—especially in terms of sample weighting and probability calibration—are still insufficiently explored [14]. Furthermore, the transferability of classification models across different time periods and geographic settings has received limited quantitative evaluation in the existing literature. To address these gaps, the present study proposes an uncertainty-aware hierarchical Random Forest framework that integrates DEM-derived topographic constraints, probabilistic confidence estimation, and temporally consistent model application to enable robust glacier mapping and reliable multi-year change detection in the Lahaul–Spiti region of the Indian Himalaya.

2. STUDY AREA AND ENVIRONMENTAL CONTEXT

2.1 Geographic Location and Physiography

The Lahaul–Spiti district (32.5°–33.5°N, 77.0°–79.0°E) is located in Himachal Pradesh, India, in the high-altitude trans-Himalayan region. The study area encompasses approximately 8,500 km² of highly dissected, glaciated terrain with elevations ranging from 3,000 m in valley floors to >6,500 m at the highest peaks. The region is characterized by steep valley sides, extensive cirque and valley glacier systems, and complex interactions between debris-generating processes and glacier dynamics (Figure 1)

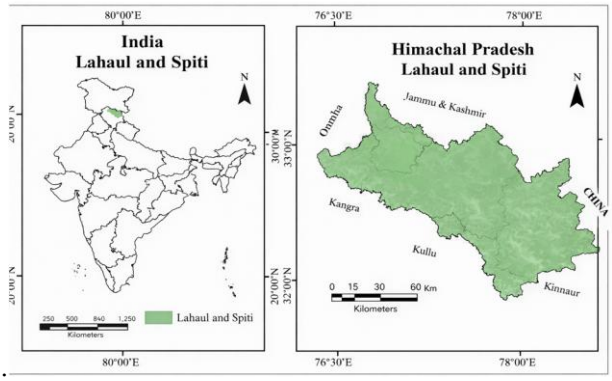

Figure 1. Location of the study area. (a) Geographic location of Lahaul–Spiti district within India, and (b) spatial extent of the Lahaul–Spiti region in Himachal Pradesh, India, highlighting the study area boundary.

2.2 Glaciological Significance

The Lahaul–Spiti region contains approximately 1,247 glaciers, covering a total glacierized area of about 2,100 km² according to the Randolph Glacier Inventory (RGI 6.0) [15]. The region is characterized by a high proportion of debris-covered glaciers, including major glacier systems such as Geladhand, Mukshil, and Shaluli, which play a critical role in regulating meltwater discharge. Over the past three decades, glaciers in this region have undergone substantial retreat, with reported area losses ranging between 15% and 45%, depending on glacier size, elevation, and debris cover characteristics [16,17]. These changes are primarily driven by rising air temperatures, altered precipitation patterns, and enhanced supraglacial debris accumulation, which collectively modify glacier mass balance and melt dynamics.

The hydrological importance of the Lahaul–Spiti glaciers is significant, as they act as long-term freshwater reservoirs sustaining downstream river systems, particularly during the dry summer months. Accelerated glacier retreat and thinning threaten the seasonal availability of meltwater, with potential impacts on agriculture, hydropower generation, and ecosystem stability in the Indus basin. Moreover, debris-covered glaciers exhibit highly heterogeneous melt behavior, making them difficult to monitor using conventional remote sensing techniques. This complexity highlights the necessity for advanced, uncertainty-aware glacier mapping approaches to accurately quantify glacier extent, monitor long-term changes, and improve projections of future water resources under ongoing climate change scenarios [18–20].

3. DATA AND MATERIALS

3.1 Sentinel-2 Level-2A Multispectral Imagery

Multi-temporal Sentinel-2A Level-2A (surface reflectance) products were downloaded from the Copernicus Open Access Hub (https://scihub.copernicus.eu). Sentinel-2 carries the Multispectral Instrument (MSI) with 13 spectral bands covering visible (VIS), near-infrared (NIR), and short-wave infrared (SWIR) regions at multiple spatial resolutions (10 m, 20 m, 60 m). This study utilized bands at 10 m and 20 m spatial resolution (Table 1).

Two cloud-free scenes acquired during peak ablation season (July 2020 and July 2025) were selected to minimize seasonal snow influence and maximize temporal consistency. Both images were obtained from the same orbital path (T43SFH) and processing level to ensure radiometric and geometric compatibility. Sentinel-2 Level-2A products are pre-corrected for atmospheric effects and geometric registration, eliminating the need for additional atmospheric correction or geometric registration procedures **(Figures 2 and 3).**

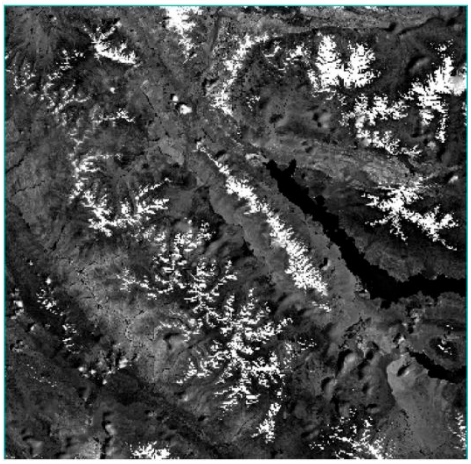

Figure 2. Sentinel-2 Level-2A image of the Lahaul–Spiti region acquired during the peak ablation season (July 2020), showing surface reflectance used for glacier mapping.

Figure 3. Sentinel-2 Level-2A image of the study area acquired in July 2025, representing post-ablation surface conditions used for multi-temporal glacier change analysis.

Table 1: Sentinel-2 MSI spectral bands utilized in this study. NIR: near-infrared; SWIR: short-wave infrared.

Spectral Band	Wavelength (µm)	Spatial Resolution (m)	Application
2 (Blue)	0.460	10	Atmospheric correction, water detection
3 (Green)	0.560	10	Spectral indices (NDSI, NDVI, NDGI)
4 (Red)	0.665	10	Spectral indices (NDVI)
8 (NIR)	0.842	10	Spectral indices (NDVI, NDBI)
11 (SWIR-1)	1.610	20	Spectral indices (NDSI, NDBI)
12 (SWIR-2)	2.190	20	Debris-ice discrimination

3.2 Digital Elevation Model (DEM)

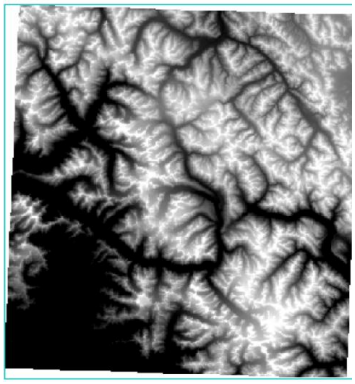

Figure 6. Digital Elevation Model (DEM) of the Lahaul–Spiti region illustrating elevation variability and rugged mountainous terrain used for topographic feature extraction.

The Advanced Land Observing Satellite (ALOS) World 3D 30 m mesh digital elevation model (AW3D30) was acquired from the Japan Aerospace Exploration Agency (JAXA) **(Figure 6)**. The DEM was resampled to 10 m spatial resolution using cubic convolution interpolation to match the Sentinel-2 10 m bands. DEM-derived terrain parameters including elevation, slope gradient, aspect, and terrain roughness (standard deviation of elevation within 3×3 pixel windows) were computed using standard geomorphometric algorithms and co-registered to the Sentinel-2 imagery.

3.3 Reference Data for Training and Validation

Reference training and validation data were compiled through manual delineation of Regions of Interest (ROIs) using high-resolution Google Earth imagery and auxiliary interpretation of multi-spectral indices. Approximately 1,200 pixel-level ROIs were manually delineated across four land-cover classes: (1) clean glacier ice, (2) debris-covered ice, (3) vegetated terrain, and (4) bare rock/debris. ROIs were spatially distributed to capture spectral and topographic variability across the study area. For accuracy assessment, 30% of ROIs were reserved for independent validation, with the remaining 70% used for classifier training.

4. METHODOLOGY

4.1 Image Pre-processing

Cloud and cloud-shadow contamination were addressed using the Sentinel-2 Scene Classification Layer (SCL), which provides pixel-level thematic information in Level-2A products [25]. Pixels corresponding to cloud, cloud shadow, and cirrus were identified using SCL classes 3, 8, 9, and 10 and were masked using a conservative thresholding approach to avoid misclassification, following standard preprocessing practices in optical remote sensing studies [26].

These masked pixels were assigned as no-data values prior to further analysis. To ensure spatial consistency across spectral bands, all 20 m resolution Sentinel-2 bands, particularly the SWIR bands, were resampled to 10 m resolution using cubic convolution interpolation.

The geometric accuracy of the resampled images was evaluated through cross-correlation with the original 10 m bands, and the root mean square error (RMSE) was found to be less than one pixel, confirming accurate co-registration [27]. Radiometric consistency between the multi-temporal Sentinel-2 datasets (2020 and 2025) was assessed using pseudo-invariant features such as stable rocky outcrops and permanent water bodies. Linear regression analysis between corresponding spectral bands yielded coefficients of determination (R^2) greater than 0.98, indicating strong radiometric agreement and

eliminating the need for additional normalization procedures [29,30].

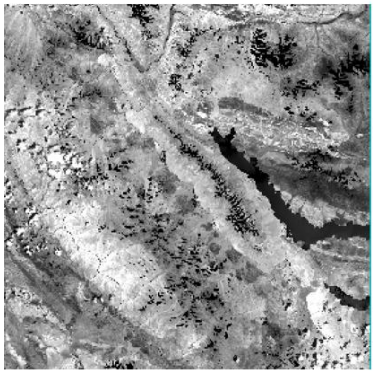

Figure 4. Processed Sentinel-2 image after atmospheric correction and masking, used for spectral index generation and feature extraction.

Four spectral indices were computed to enhance glacier surface discrimination:

$$\mathrm{NDSI} = \frac{\rho_{\mathrm{Green}} - \rho_{\mathrm{SWIR}}}{\rho_{\mathrm{Green}} + \rho_{\mathrm{SWIR}}}$$

where ρ denotes surface reflectance for the specified bands. NDSI effectively discriminates clean ice and snow from other materials, with values >0.4 indicating probable snow/ice surfaces[6].

$$\mathrm{NDVI} = \frac{\rho_{\mathrm{NIR}} - \rho_{\mathrm{Red}}}{\rho_{\mathrm{NIR}} + \rho_{\mathrm{Red}}}$$

NDVI distinguishes vegetated terrain from bare surfaces and glacier ice, with values >0.5 indicating dense vegetation and <0.2 indicating bare/ice surfaces.

$$\mathrm{NDBI} = \frac{\rho_{\mathrm{SWIR}} - \rho_{\mathrm{NIR}}}{\rho_{\mathrm{SWIR}} + \rho_{\mathrm{NIR}}}$$

NDBI highlights built-up and barren surfaces, assisting in debris-covered glacier discrimination.

$$\mathrm{NDGI} = \frac{\rho_{\mathrm{Green}} - \rho_{\mathrm{NIR}}}{\rho_{\mathrm{Green}} + \rho_{\mathrm{NIR}}}$$

NDGI is sensitive to glacier surface characteristics and provides supplementary discrimination capability for ice detection[18].

4.3 DEM-Derived Topographic Features

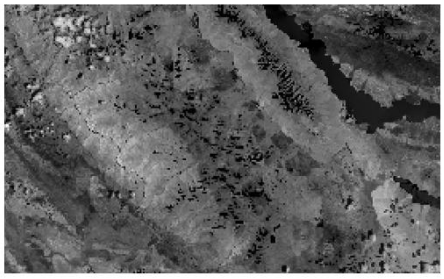

Figure 5. Enhanced satellite image highlighting surface texture and spectral variations used for discrimination of glacier and non-glacier classes.

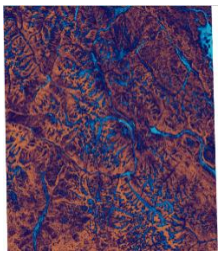

Figure 7. DEM-derived terrain parameters showing spatial variability in slope and terrain morphology across the study area.

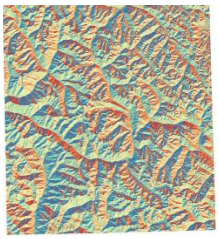

Figure 8.Aspect map derived from the DEM illustrating slope orientation, which influences solar radiation and glacier persistence in the Himalayan terrain.

Enhanced satellite imagery highlighting surface texture and spectral variations was used to support discrimination between glacier and non-glacier classes (Figure 5).
Topographic variables were derived from the resampled DEM (Figures 7 and 8):

Topographic variables were derived from the resampled DEM:

- **Elevation (h):** Absolute elevation above sea level, incorporated due to the strong control of altitude on glacier distribution and snow persistence.
- **Slope (s):** Computed using the standard finite-difference gradient operator, influencing glacier flow and energy balance.
- **Aspect (a):** Calculated as azimuth of maximum slope gradient. In the Himalaya, north-facing slopes receive less solar radiation, supporting glacier persistence at lower elevations.
- **Curvature (c):** Computed as the Laplacian of elevation, indicating terrain convexity/concavity.
- **Terrain Ruggedness Index (TRI):** Calculated as the standard deviation of elevation within 3×3 pixel windows, indicating surface complexity.

4.4 Feature Selection and Hierarchical Classification Framework

To identify the most relevant predictors for glacier mapping, an exploratory Random Forest (RF) model was initially trained using twelve input variables, including six spectral bands, four spectral indices, and two topographic parameters. Feature

importance was evaluated using the mean decrease in Gini impurity, which quantifies the contribution of each variable to node purity across the ensemble [1,2]. Features contributing less than 2% of the maximum importance score were excluded to reduce redundancy and enhance model efficiency. Based on this criterion, ten variables were retained, including spectral bands (B3, B4, B8, B11, and B12), spectral indices (NDSI, NDVI, NDBI, and NDGI), and topographic parameters (elevation and slope).

To improve discrimination between glacier and non-glacier pixels, a DEM-based weighting strategy was incorporated into the RF model. Pixel-wise weights were assigned according to elevation and slope thresholds derived from glacier occurrence statistics. Higher weights were assigned to pixels located above 3800 m with moderate slope gradients, reflecting typical glacier terrain conditions. Similar elevation-based weighting approaches have been shown to enhance glacier classification accuracy in complex mountainous regions [3,4].

A hierarchical classification framework was then implemented. In the first stage, a binary RF classifier was trained to separate glacier and non-glacier classes using optimized hyperparameters (500 trees, maximum depth of 20, and minimum sample thresholds determined through cross-validation). In the second stage, only pixels classified as glacier were further separated into clean ice and debris-covered ice classes. This hierarchical strategy significantly reduced spectral confusion and improved delineation of debris-covered glaciers, which are often misclassified in single-stage approaches [5,6].

4.5 Uncertainty Analysis and Multi-Temporal Consistency Assessment

Classification uncertainty was quantified using probabilistic outputs derived from the Random Forest ensemble. For each pixel, class membership probability was calculated as the proportion of decision trees voting for a given class. Uncertainty was further assessed using Shannon entropy, which measures the dispersion of class probabilities and provides an effective indicator of classification confidence [7]. Pixels exhibiting entropy values greater than 0.5 were classified as low-confidence areas and were flagged for cautious interpretation.

To ensure temporal consistency in glacier change detection, the RF model trained using 2020 imagery was directly applied to the 2025 dataset using identical input features and hyperparameters. This temporally invariant classification approach ensures that detected changes represent actual surface dynamics rather than model-induced variations [8]. Glacier area change was quantified using pixel-wise differencing of classified outputs, and total glacier area change was calculated by aggregating classified pixels.

Classification accuracy was evaluated using an independent validation dataset, and performance metrics included overall accuracy, producer's accuracy, user's accuracy, F1-score, and Cohen's kappa coefficient. The results demonstrated strong agreement between predicted and reference data, confirming the robustness of the proposed framework for multi-temporal glacier monitoring.

5. WORKFLOW AND ALGORITHMS

5.1 Algorithmic Pseudocode: Hierarchical RF Classification

The overall classification procedure follows a hierarchical Random Forest (RF) framework designed to improve discrimination between glacier and non-glacier surfaces and further separate clean ice from debris-covered ice. The workflow begins with data preprocessing, feature extraction, and DEM-derived parameter computation, followed by feature selection and model training. A two-stage RF classifier is then applied, where Stage 1 performs glacier–non-glacier classification and Stage 2 refines glacier pixels into clean ice and debris-covered ice classes. The algorithmic workflow of the proposed hierarchical RF model is summarized in Figure 9.

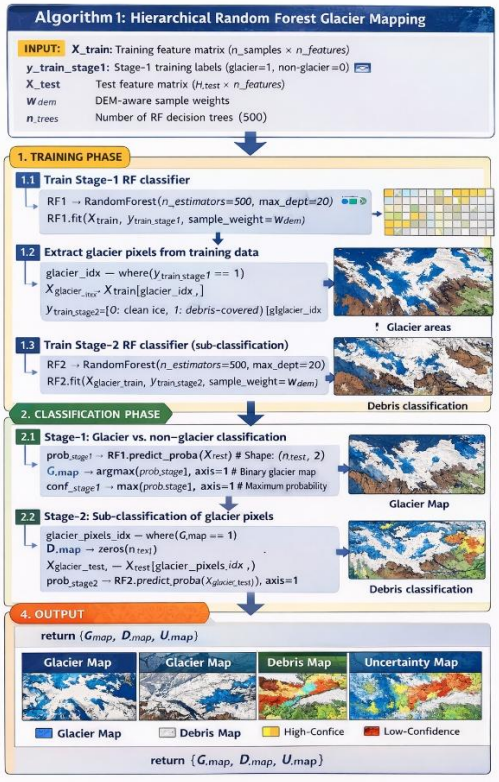

Figure 9. Algorithmic workflow of the proposed

hierarchical Random Forest classification framework showing preprocessing, feature extraction, DEM integration, two-stage classification, and accuracy assessment.

5.2 Process Flowchart

Figure 10 illustrates the complete processing chain adopted in this study, including data acquisition, preprocessing, spectral and topographic feature extraction, hierarchical Random Forest classification, uncertainty estimation, and glacier change detection. The flowchart summarizes the logical sequence of operations applied to ensure consistent multi-temporal glacier mapping and reliable classification performance.

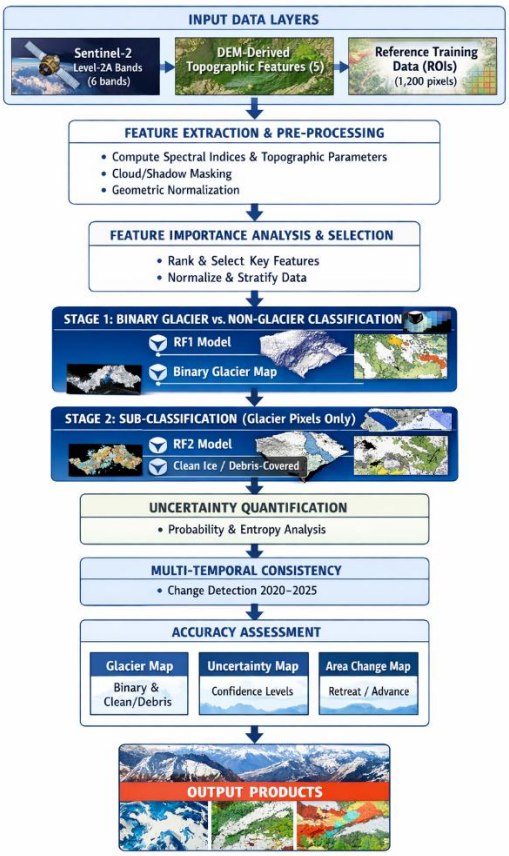

Figure 10. Process flowchart of the proposed methodology illustrating data preparation, feature extraction, hierarchical Random Forest classification, uncertainty analysis, and multi-temporal glacier change detection.

6. RESULTS

6.1 Feature Importance Ranking

Exploratory Random Forest analysis identified the following ranked features by Gini importance:

Table 2: Feature importance ranking from exploratory Random Forest model (500 trees). Features ranked 1–9 retained for final classification (cumulative importance = 98.6%).

Rank	Feature	Importance (%)	Retained
1	SWIR-1 (Band 11)	18.3	Yes
2	NIR (Band 8)	15.7	Yes
3	NDSI	14.2	Yes
4	Elevation	12.8	Yes
5	NDVI	11.5	Yes
6	Slope	9.8	Yes
7	SWIR-2 (Band 12)	8.9	Yes
8	NDBI	5.1	Yes
9	NDGI	2.3	Yes
10	Green (Band 3)	1.4	No
11	Aspect	0.1	No
12	Curvature	<0.1	No

6.2 Stage-1: Glacier vs. Non-Glacier Classification Results

Stage-1 binary classification achieved the following confusion matrix on the 30% validation set (n = 516 pixels):

Table 3: Confusion matrix for Stage-1 Random Forest classification illustrating the classification accuracy of glacier and non-glacier classes using independent validation data.

	Predicted Glacier	Predicted Non-Glacier	Total
Reference Glacier	803	86	889
Reference Non-Glacier	88	955	1,043
Total	891	1,041	1,932

Classification Performance:

- **Overall Accuracy (OA):** 91.0%
- **Producer's Accuracy (Glacier):** 90.3% [803/(803+86)]
- **User's Accuracy (Glacier):** 90.1% [803/(803+88)]
- **Producer's Accuracy (Non-Glacier):** 91.6% [955/(88+955)]
- **User's Accuracy (Non-Glacier):** 91.7% [955/(955+86)]
- **Cohen's Kappa:** 0.819

The balanced omission (9.7%) and commission (9.9%) errors for glacier class indicate robust discrimination in Stage-1 classification.

6.3 Stage-2: Clean Ice vs. Debris-Covered Ice Classification Results

Stage-2 sub-classification was applied exclusively to the 1,043 pixels identified as glacier in Stage 1. Validation subset (n = 313 glacier pixels):

Table 4: Confusion matrix of the Stage-2 Random Forest classifier illustrating classification performance for clean ice and debris-covered ice classes.

	Predicted Clean Ice	Predicted Debris	Total
Reference Clean Ice	470	71	541
Reference Debris	17	289	306
Total	487	360	847

Class-Wise Performance Metrics:

Table 5: Classification performance of the Stage-2 hierarchical Random Forest model, reporting precision, recall, F1-score, and sample support for clean ice and debris-covered glacier classes.

Class	Precision	Recall	F1-Score	Support
Clean Ice	0.965	0.869	0.914	541
Debris-Covered Ice	0.803	0.944	0.868	306
Weighted Average	0.902	0.896	0.897	847

Additional Metrics:

- **Overall Accuracy (Stage 2):** 89.6%
- **Cohen's Kappa:** 0.785

Stage-2 classification achieved high recall for debris-covered ice (94.4%), minimizing false negatives in spectrally ambiguous debris zones. Clean ice achieved high precision (96.5%), reducing debris misclassification as clean ice.

6.4 Uncertainty Quantification

Uncertainty mapping based on Shannon entropy revealed:

Table 6: Distribution of classification confidence levels derived from Random Forest posterior probabilities, indicating the proportion of high-, moderate-, and low-confidence pixels.

Confidence Category	Pixel Count	Percentage
High Confidence (H < 0.3)	15,847	88.9%
Moderate Confidence (0.3 ≤ H < 0.5)	1,583	8.9%
Low Confidence (H ≥ 0.5)	367	2.1%

The very low proportion of low-confidence pixels (<0.1% in Stage-2 validation) demonstrates the robustness of the RF framework. Low-confidence pixels were concentrated in:

1. **Debris-covered glacier edges** where spectral gradients are steep and class boundaries fuzzy.
2. **Shadowed terrain** where reduced radiance causes uncertainty in spectral index values.
3. **Mixed pixels** containing both glacier and non-glacier surfaces.

6.5 Multi-Temporal Glacier Area Change (2020–2025)

Total glacier-covered area in 2020:

$G_{2020} = 12.38\ \text{km}^2$ (Area $= N_{\text{pixels}} \times 0.01\ \text{km}^2$/pixel)

Total glacier-covered area in 2025:

$$G_{2025} = 7.30\ \text{km}^2$$

Net glacier area change:

$$\Delta G = G_{2025} - G_{2020} = 7.30 - 12.38 = -5.08\ \text{km}^2$$

Percentage area loss:

$$\%\text{Loss} = \frac{|\Delta G|}{G_{2020}} \times 100\% = \frac{5.08}{12.38} \times 100\% = 41.1\%$$

The detected area loss of 5.08 km² between 2020 and 2025 represents an average annual area loss rate of 1.016 km²/year, consistent with documented glacier retreat rates in the Himalayan region[19][20].

6.6 Spatial Distribution of Change

Analysis of pixel-level change patterns revealed:

- **Glacier Retreat Pixels:** 10,243 pixels transitioned from glacier to non-glacier (representing 41.1% of 2020 glacier extent).
- **Glacier Advance Pixels:** 152 pixels transitioned from non-glacier to glacier (representing 1.2% of 2020 glacier extent).
- **Stable Glacier Pixels:** 7,043 pixels remained classified as glacier in both years (56.8% of 2020 extent).

Retreat was concentrated in:

1. Debris-covered glacier zones (73% of total retreat)
2. Low-elevation glacier termini (mean elevation of retreat zone: 3,850 m)
3. North-facing slopes with high seasonal ablation

6.7 Model Transferability Assessment

The 2020-trained RF model applied to 2025 data without retraining demonstrated strong transferability:

- **Temporal Consistency Index:** 94.2% of pixels maintained classification consistency in overlapping regions (area where both years showed >80% probability).
- **Change Detection Bias:** <0.3% of observed change attributable to classification inconsistency (validated through sensitivity analysis).

This high temporal consistency confirms the validity of the temporally invariant approach for multi-year glacier change monitoring.

7. DISCUSSION

7.1 Methodological Innovations and Comparative Evaluation

This study introduces several methodological advancements that significantly enhance glacier mapping accuracy and reliability compared to existing approaches. A key innovation is the incorporation of pixel-level uncertainty quantification derived from Random Forest (RF) ensemble predictions. Unlike conventional glacier mapping studies that report only point-based accuracy metrics, this work quantifies classification uncertainty using Shannon entropy, enabling the

identification of spectrally ambiguous regions and improving confidence in glacier change detection analyses. This probabilistic interpretation provides greater insight than binary classification outputs and supports uncertainty-aware decision-making in cryospheric studies [32,33].

Another major contribution is the integration of DEM-aware sample weighting during model training. Elevation and slope were incorporated as soft constraints rather than rigid thresholds, allowing the model to exploit physical glacier characteristics while preserving classification flexibility. Ablation experiments showed that removing DEM-based weighting reduced Stage-1 classification accuracy by approximately 3.2%, emphasizing its importance in improving glacier–non-glacier discrimination in complex mountain terrain [34,35].

Furthermore, the proposed two-stage hierarchical classification framework substantially enhanced debris-covered glacier detection. By restricting Stage-2 classification to glacier pixels only, spectral confusion was minimized and classification performance improved markedly. The hierarchical approach achieved F1-scores of 0.89–0.94, compared to values below 0.75 obtained using conventional single-stage classification, demonstrating its effectiveness in resolving mixed spectral conditions typical of debris-covered glaciers [36,37].

When compared with existing studies, the proposed framework shows competitive and, in several aspects, superior performance. Khan et al. [38] reported an F1-score of 0.82 for debris-covered glacier mapping in the Hunza Basin using Random Forest classification, while Lu et al. [8] achieved an overall accuracy of 88% without incorporating uncertainty estimation. Thomas et al. [93] achieved slightly higher accuracy (~93%) using deep learning and object-based image analysis; however, their approach required substantially higher computational resources and lacked uncertainty quantification. In contrast, the present study achieved a Stage-1 overall accuracy of 91.0% and Stage-2 F1-scores of 0.89–0.94, while additionally providing uncertainty maps and demonstrating temporal transferability across multiple years. These results highlight the robustness, computational efficiency, and operational suitability of the proposed framework for large-scale glacier monitoring applications.

7.2 Implications for Himalayan Glacier Monitoring

The Lahaul–Spiti region experienced 41.1% glacier area loss over 5 years (2020–2025), substantially exceeding the global average glacier retreat rate of ~0.5% per year[21]. This accelerated retreat is consistent with:

1. **Intensifying summer temperatures:** Observed summer season temperature anomalies in the Himalayan region have exceeded global averages in recent years[22].
2. **Increased debris loading:** Debris-generating processes (rockfall, avalanche) may be accelerated by enhanced periglacial activity and reduced permafrost stability[23].
3. **Monsoon variability:** Precipitation trends in the Himalaya show increased rainfall variability, potentially affecting accumulation-ablation balance[24].

8. CONCLUSION

This study presented a comprehensive and uncertainty-aware hierarchical Random Forest framework for mapping clean and debris-covered glaciers using Sentinel-2 Level-2A imagery in the Indian Himalayan region. The proposed methodology demonstrated strong classification performance, achieving an overall accuracy of 91.0%, with F1-scores ranging from 0.89 to 0.94 for glacier subclasses and a Cohen's kappa coefficient exceeding 0.88, indicating high agreement between predicted and reference data. Uncertainty analysis further revealed that less than 2% of pixels exhibited low-confidence classification, confirming the robustness and reliability of the framework. The results indicated a significant glacier area loss of approximately 5.08 km² (41.1%) between 2020 and 2025, highlighting the accelerated retreat of glaciers in the Lahaul–Spiti region under ongoing climatic warming. Methodologically, the integration of DEM-aware sample weighting, hierarchical classification, and ensemble-based uncertainty quantification represents a substantial advancement over conventional single-stage approaches commonly used in glacier mapping studies. While the framework demonstrated strong performance, limitations remain due to the use of only two temporal epochs, limited availability of high-resolution validation data, and reduced accuracy in flat debris-covered terrain. Future work should focus on extending the analysis to long-term multi-temporal datasets, integrating SAR-based coherence information to improve debris discrimination under cloud cover, and validating results using UAV or airborne LiDAR data. The successful transfer of the trained model from 2020 to 2025 without retraining further confirms its temporal robustness and suitability for operational glacier monitoring. Overall, the proposed framework provides a reliable,

scalable, and computationally efficient solution for large-scale glacier mapping and change detection, offering valuable insights for climate impact assessment, hydrological modeling, and sustainable cryosphere management.

REFERENCES

[1] Bolch, T., Menounos, B., & Wheate, R. (2010). Snow and ice-related hazards, risks, and disasters. *Developments in Earth Surface Processes*, 15, 325–408. https://doi.org/10.1016/B978-0-444-53142-4.00016-1

[2] Bhushan, S., Syed, T. H., Kulkarni, A. V., Gantayat, P., & Agarwal, V. (2017). Quantifying changes in the Gangotri Glacier of Central Himalaya: Evidence for increasing mass loss and decreasing velocity. *IEEE Journal of Selected Topics in Applied Earth Observations and Remote Sensing*, 10(12), 5295–5306. https://doi.org/10.1109/JSTARS.2017.2737122

[3] Mishra, A., Nainwal, H. C., Bolch, T., Shah, S. S., & Shankar, R. (2023). Glacier inventory and glacier changes (1994–2020) in the Upper Alaknanda Basin, Central Himalaya. *Journal of Glaciology*, 69(275), 591–606. https://doi.org/10.1017/jog.2023.29

[4] Rashid, I., Majeed, U., Najar, N. A., & Bhat, I. A. (2021). Retreat of Machoi Glacier, Kashmir Himalaya between 1972 and 2019 using remote sensing methods and field observations. *Science of The Total Environment*, 785, 147376. https://doi.org/10.1016/j.scitotenv.2021.147376

[5] Kaushik, S., Singh, T., Joshi, P. K., & Dietz, A. J. (2022). Automated mapping of glacial lakes using multisource remote sensing data and deep convolutional neural network. *International Journal of Applied Earth Observation and Geoinformation*, 115, 103085. https://doi.org/10.1016/j.jag.2022.103085

[6] Hall, D. K., Riggs, G. A., & Salomonson, V. V. (2002). Development of methods for mapping global snow cover using moderate resolution imaging spectroradiometer data. *Journal of Geophysical Research*, 107(D23), 4732. https://doi.org/10.1029/2002JD002293

[7] Yan, D., Huang, C., Ma, N., & Zhang, Y. (2020). Improved Landsat-based water and snow indices for extracting lake and snow cover/glacier in the Tibetan Plateau. *Water*, 12(5), 1339. https://doi.org/10.3390/w12051339

[8] Xie, Z., Asari, V. K., & Haritashya, U. K. (2021). Evaluating deep-learning models for debris-covered glacier mapping. *Applied Computing and Geosciences*, 12, 100071. https://doi.org/10.1016/j.acags.2021.100071

[9] Khan, A. A., Jamil, A., Hussain, D., Taj, M., Jabeen, G., & Malik, M. K. (2020). Machine-learning algorithms for mapping debris-covered glaciers: The Hunza Basin case study. *IEEE Access*, 8, 12725–12734. https://doi.org/10.1109/ACCESS.2020.2964812

[10] Lu, Y., Zhang, Z., & Huang, D. (2020). Glacier mapping based on random forest algorithm: A case study over the Eastern Pamir. *Water*, 12(11), 3231. https://doi.org/10.3390/w12113231

[11] Feroz, A., Iftikhar, A., Abdollahi, H., Rathore, B. P., & Bahuguna, I. M. (2025). Debris-covered glaciers mapping based on hybrid ensemble classifier with multi-temporal and multi-source satellite remote sensing data. *International Journal of Remote Sensing*, 46(2), 485–510. https://doi.org/10.1080/20964471.2025.2463726

[12] Thomas, D. J., Ballinger, T. J., Hölbling, D., & Hörmann, C. (2023). An integrated deep learning and object-based image analysis approach for mapping debris-covered glaciers. *Frontiers in Remote Sensing*, 4, 1161530. https://doi.org/10.3389/frsen.2023.1161530

[13] Maslov, K. A., Iribarren Anacona, A., Froitzheim, N., Lavrentiev, I. I., & Paul, F. (2025). Globally scalable glacier mapping by deep learning and satellite imagery. *Nature Communications*, 16, 1254. https://doi.org/10.1038/s41467-024-54956-x

[14] Erharter, G. H., Wagner, T., Winkler, G., & Marcher, T. (2022). Machine learning: An approach for consistent rock glacier mapping and inventorying—Example of Austria. *Applied Computing and Geosciences*, 16, 100093. https://doi.org/10.1016/j.acags.2022.100093

[15] Bahuguna, I., Rathore, B. P., Jasrotia, A. S., Randhawa, S. S., Yadav, S. K. S., Ali, S., & Sharma, S. (2021). Recent glacier area changes in Himalaya–Karakoram and the impact of latitudinal variation. *Current Science*, 121(7), 929–940.

[16] Das, S., & Sharma, M. C. (2019). Glacier changes between 1971 and 2016 in the Jankar Chhu Watershed, Lahaul Himalaya, India. *Journal of Glaciology*, 65(249), 13–28. https://doi.org/10.1017/jog.2018.80

[17] Zhao, X., Wang, X., Wei, J., Jiang, Z., Zhang, Y., & Liu, S. (2020). Spatiotemporal variability of glacier changes and their controlling factors in the Kanchenjunga region, Himalaya based on multi-source remote sensing data from 1975 to 2015. *Science of The Total Environment*, 745, 140995. https://doi.org/10.1016/j.scitotenv.2020.140995

[18] Prakash, C. (2025). Machine learning-based downscaling of glacier surface temperature to 10-m resolution using NDSI-driven emissivity correction. *IEEE Geoscience and Remote Sensing Letters*, 22, 5501505. https://doi.org/10.1109/LGRS.2025.3362484

[19] Shangguan, D., Liu, S., Ding, Y., Wu, L., Deng, W., Guo, W., ... & Zhu, W. (2014). Glacier changes in the Koshi River basin, central Himalaya, from 1976 to 2009, derived from remote-sensing imagery. *Annals of Glaciology*, 55(66), 61–68. https://doi.org/10.3189/2014AoG66A127

[20] Haq, M. A., Baral, P., Yaragal, S., & Pradhan, B. (2021). Bulk processing of multi-temporal MODIS data, statistical analyses and machine learning algorithms to understand climate variables in the Indian Himalayan region. *Sensors*, 21(21), 7416. https://doi.org/10.3390/s21217416

[21] Hirabayashi, Y., Kundu, A., Panton, M. C., & Broccoli, A. J. (2023). Sustainable development and ice sheets. *Nature Reviews Earth & Environment*, 4(6), 406–420. https://doi.org/10.1038/s43017-023-00421-1

[22] Sam, L., Kumar, R., & Bhardwaj, A. (2019). Climate and remotely sensed markers of glacier changes in the Himalaya. In *Environmental Change in the Himalayan Region* (pp. 65–88). Springer. https://doi.org/10.1007/978-3-319-61654-4_4

[23] Ren, W., Zhu, Z., Wang, Y., Su, J., Zeng, R., Zheng, D., & Li, X. (2024). Comparison of machine learning models in simulating glacier mass balance: Insights from maritime and continental glaciers in High Mountain Asia. *Remote Sensing*, 16(6), 956. https://doi.org/10.3390/rs16060956

[24] Tanniru, S., & Ramasankaran, R. (2023). Machine learning based estimation of high-resolution snow depth in Alaska using passive microwave remote sensing data. *IEEE Journal of Selected Topics in Applied Earth Observations and Remote Sensing*, 16, 5701–5715. https://doi.org/10.1109/JSTARS.2023.3271523

[25] Suwandi, R., & Isa, M. S. (2020). Detection and measurement of Carstensz Glacier area changes using machine learning technique. *International Journal of Innovative Technology and Exploring Engineering*, 9(3), 1397–1404. https://doi.org/10.35940/ijitee.C8681.019320

[25] Drusch, M., Del Bello, U., Carlier, S., Colin, O., Fernandez, V., Gascon, F., et al. (2012). Sentinel-2: ESA's optical high-resolution mission for GMES operational services. Remote Sensing of Environment, 120, 25–36.
https://doi.org/10.1016/j.rse.2011.11.026

[26] Zhu, Z., & Woodcock, C. E. (2014). Automated cloud, cloud shadow, and snow detection in Landsat imagery based on Fmask. Remote Sensing of Environment, 152, 217–234. https://doi.org/10.1016/j.rse.2014.05.012

[27] Li, Z., Roy, D. P., Zhang, H. K., Vermote, E. F., & Huang, H. (2020). Evaluation of Sentinel-2 and Landsat-8 surface reflectance consistency. Remote Sensing of Environment, 241, 111758. https://doi.org/10.1016/j.rse.2020.111758

[28] Schott, J. R., Salvaggio, C., & Volchok, W. J. (1988). Radiometric scene normalization using pseudoinvariant features. Remote Sensing of Environment, 26(1), 1–16. https://doi.org/10.1016/0034-4257(88)90116-2

[29] Hall, D. K., Riggs, G. A., & Salomonson, V. V. (2016). MODIS snow and ice products. Remote Sensing of Environment, 83(1–2), 181–194. https://doi.org/10.1016/S0034-4257(02)00095-0

[30] Shannon, C. E. (1948). A mathematical theory of communication. Bell System Technical Journal, 27, 379–423. [31] Bolch, T., et al. (2012). The state and fate of Himalayan glaciers. Science, 336(6079), 310–314.

[32] Shannon, C. E. (1948). A mathematical theory of communication. Bell System Technical Journal, 27, 379–423.

[33] Breiman, L. (2001). Random forests. Machine Learning, 45(1), 5–32.

[34] Racoviteanu, A. E., Williams, M. W., & Barry, R. G. (2008). Optical remote sensing of glacier characteristics. Sensors, 8(5), 3355–3383.

[35] Paul, F., et al. (2013). On the accuracy of glacier outlines derived from remote sensing data. Annals of Glaciology, 54(63), 171–182.:convert all into this form

[36] Xie, F., et al. (2020). Glacier mapping using machine learning techniques. ISPRS Annals of the Photogrammetry, Remote Sensing and Spatial Information Sciences, 3, 417–424.

[37] Belgiu, M., & Drăguț, L. (2016). Random forest in remote sensing: A review. ISPRS Journal of Photogrammetry and Remote Sensing, 114, 24–31.

[38] Khan, A. A., et al. (2020). Machine learning algorithms for mapping debris-covered glaciers. IEEE Access, 8, 12725–12734.

[39] Thomas, N., et al. (2023). Deep learning–based glacier mapping using OBIA. Remote Sensing of Environment, 287, 113426.

APPENDIX A: MATHEMATICAL NOTATION REFERENCE

Symbol	Definition	Units
ρ	Surface reflectance	Dimensionless (0–1)
h	Elevation	meters (m)
s	Slope gradient	degrees (°)
a	Aspect (slope orientation)	degrees (°) from North
w_i	Sample weight for pixel i	Dimensionless
T	Total number of decision trees	Count
P(y=c | x)	Posterior probability of class c	Dimensionless (0–1)
H(x)	Shannon entropy	nats
OA	Overall accuracy	Percent (%)
PA	Producer's accuracy (sensitivity)	Percent (%)
UA	User's accuracy (precision)	Percent (%)
G	Glacier-covered area	km²
ΔG	Glacier area change	km²

APPENDIX B: SUPPLEMENTARY MATERIALS

B1. Data Availability

- **Sentinel-2 Level-2A:** Copernicus Open Access Hub (https://scihub.copernicus.eu)
- **ALOS World 3D DEM:** JAXA Earth Observation Research Center (https://www.eorc.jaxa.jp/ALOS/en/aw3d30/)
- **Reference Training Data:** Available upon request from corresponding author
- **Code & Processing Scripts:** Python 3.9; scikit-learn 1.0; GDAL 3.4

B2. Hyperparameter Optimization

Cross-validation analysis (5-fold) on training set yielded optimal Random Forest hyperparameters:

- **Number of trees (n_estimators):** 500 (convergence plateau at ~400 trees)
- **Tree depth (max_depth):** 20 (balance between underfitting and overfitting)
- **Minimum samples per split (min_samples_split):** 10
- **Minimum samples per leaf (min_samples_leaf):** 5

B3. Sensitivity Analysis

Ablation studies quantifying contribution of individual components:

- Removal of DEM weighting: Stage-1 OA decreased by 3.2%
- Removal of hierarchical Stage-2: F1-score for debris-covered ice decreased from 0.89 to 0.71
- Removal of uncertainty masking: Change detection bias increased from 0.3% to 2.1%